Composites: Part A 40 (2009) 1621–1631

Contents lists available at ScienceDirect

Composites: Part A

journal homepage: www.elsevier.com/locate/compositesa

Interlaminar fracture analysis in the G_I–G_{III} plane using prestressed transparent composite beams

András Szekrényes *

Department of Applied Mechanics, Budapest University of Technology and Economics, H-1111 Budapest, Műegyetem rkp. 5, Building MM, Hungary

ARTICLE INFO

Article history:
Received 9 April 2009
Received in revised form 17 July 2009
Accepted 17 July 2009

Keywords:
A. Glass fibres
B. Delamination
C. Analytical modeling
D. Mechanical testing

ABSTRACT

In this paper the mixed-mode I/III prestressed split-cantilever beam fracture specimen is developed, which combines the mode-III modified split-cantilever beam and the well-known double-cantilever beam specimens using a special rig. The most important feature of the novel beam-like specimen is that it is able to provide any combination of the mode-I and mode-III energy release rates. First, the mode-I part of the energy release rate is fixed by inserting a steel roller between the specimen arms inducing a fixed crack opening displacement. Second, the mode-III part of the energy release rate is provided by the external load using a special rig. A simple closed-form solution is developed using beam theory as a data reduction scheme and for the calculation of the energy release rates of the new configuration. The applicability and the limitations of the novel fracture mechanical test are demonstrated using unidirectional glass/polyester composite specimens. If only crack propagation onset is involved then the mixed-mode I/III prestressed split-cantilever beam specimen can be used to obtain the fracture criterion of transparent composite materials in the G_I–G_{III} plane in a relatively simple way.

1. Introduction

One of the most important damage mechanisms in laminated composite materials is the interlaminar fracture (also known as delamination fracture). Considering the linear elastic fracture mechanics (LEFM), e.g. [1] three basic types of the interlaminar fracture are known: mode-I (opening), mode-II (sliding or in-plane shear) and the mode-III (tearing or anti-plane shear). The major part of the literature deals with the mode-I, mode-II and the mixed-mode I/II cases. Furthermore, the mode-III fracture has also a great interest in the composite sciences. Considering the available fracture mechanical configurations for the investigation of mode-I, mode-II and mixed-mode I/II cases extensive reviews have been included in some recent papers [2,3] and so here we do not go into details in this respect.

In the field of the mode-III delamination there is a definite progress including the application of some existing specimen types and the development of new test methods. One of the earliest mode-III test developments are the split-cantilever beam (SCB) [4–6] which incorporates loading parallel to the delamination plane and the so-called crack rail shear (CRS) specimens [7]. Due to the significant mode-II component and the high stiffness both were abandoned. Later Robinson and Song [8] proposed the loading scheme necessary to reduce the mode-II component in the SCB specimen, while implementing their idea Cicci et al. [9], Sharif et al. [10] and Trakas and Kortschot [11] constructed a special rig (modified split-cantilever beam – MSCB) realizing a mode-III dominant fracture. The modified rig was recently applied by Rizov et al. [12]. The anti-clastic plate bending (ACPB) has also been applied to the determination of the mode-III fracture toughness [13,14]. None of the mentioned systems became successful in the fracture mechanics due to data reduction and other problems.

The edge-crack torsion (ECT) specimen was developed by Lee [15]. It is considered to be a very important contribution to the mode-III fracture developments [16,17]. In a recent study Ratcliffe [18] showed some drawbacks of the ECT test: dependence of the critical ERR on the crack length, deviation of the load–displacement curves from linearity and damage of the specimen before delamination failure. Recently, the ECT test was applied by Pennas and Cantwell [19] and Morais et al. [20] who showed (corresponding with the results by Ratcliffe [18]) that the mode-III critical ERR increases with the crack length. Recently, Moura et al. [21] elaborated that the increase of the toughness with the crack length is due to the fact that the crack does not propagate uniformly between the loading pins and the damaged area at peak load increases with the initial crack length.

There are also some other systems, like the splitting specimen by Ehart et al. [22,23], and the mode-III version of the four point bend end-notched flexure (4ENF) specimen [24], but these do not seem to be the optimal solutions for composites.

The literature contains only few papers, which present experimental and theoretical analyses on the mixed-mode I/III and II/III fracture, furthermore most of the relevant papers present

* Tel.: +36 1 463 1170; fax: +36 1 463 3471.
E-mail address: szeki@mm.bme.hu

1359-835X/$ - see front matter © 2009 Elsevier Ltd. All rights reserved.
doi:10.1016/j.compositesa.2009.07.009

experimental results performed on different types of metals [25–27]. For the mixed-mode I/III fracture testing of composites materials the so-called 8-point bending plate test (8PBP) was proposed by Pereira and de Morais [28]. They developed also the 6-point bend plate (6PBP) [29] for the mixed-mode II/III delamination characterization of composite laminates. Both tests are based on the bending of cross-ply composite plates. These systems are useful, however the energy release rate can be evaluated only by a numerical model and the crack initiation is expected at several (2 and 4) points simultaneously. Finally the applied plate geometry differs significantly from that of the common double-cantilever beam (DCB) and end-notched flexure (ENF) specimens. Another mixed-mode II/III specimen type is the prestressed end-notched flexure ($PENF_{II/III}$) [30] system which is the combination of the mode-II ENF and the mode-III MSCB. The method uses a special rig to increase the mode-III energy release rate by preloading the specimen and by using a three-point bending setup the mode-II ERR is provided by a simple loading head. A relatively simple beam theory scheme was found to be accurate for the data evaluation.

The main goal of this work is the development of a mixed-mode I/III delamination testing system, called the prestressed split-cantilever beam ($PSCB_{I/III}$). Based on two former works [30,31] the combination of the mode-I DCB and the mode-III MSCB specimen is necessary. The new configuration is analyzed using beam and finite element models, respectively. In accordance with the 3D finite element analysis the mode ratio changes significantly along the crack front. Furthermore, experiments on glass/polyester composite specimens are also performed. The measured data is reduced by improved beam theory (IBT) and the direct beam theory (DBT) methods. Based on the experiments the fracture envelope in the G_I–G_{III} plane is constructed for the present material. An important conclusion is that there is certain interaction between the mode-I and mode-III ERRs. It is also important to note that at each measured point there is a little mode-II contribution to the total energy release rate; however it can be reduced to 2–6% depending on the ratio of G_I and G_{III}. Finally the obtained fracture envelope is compared to those in the G_I–G_{II} and G_{II}–G_{III} planes.

2. The PSCB specimen for mixed-mode I/III cracking

The $PSCB_{I/III}$ specimen is the combination of the DCB and MSCB specimens. As it is shown in Fig. 1 P_{DCB} is load related to the mode-I part of the ERR caused by the steel roller, while P_1 and P_2 are the load values related to the mode-III loading. Based on the equilibrium of the system we have: $P_1 = P_{MSCB} \cdot s_2/s_1$ and $P_2 = P_{MSCB} \cdot (1 + s_2/s_1)$, where P_{MSCB} is the load related to the mode-III fracture, s_1 and s_2 are the distances between rollers A, B and C (see Fig. 2). Fig. 2 shows the 2D view of the prestressed specimen and the loading grips. The mode-I part of the ERR is fixed by using a steel roller. In order to make a mixed-mode I/III system, we put a prestressed DCB specimen (Fig. 1a) into the rig shown in Fig. 2.

The loading rigs transfer a scissor-like load to the prestressed specimen through rollers A and B, while the external load, P_{MSCB} is introduced through roller C using a testing machine. Due to the steel roller inserted between the delamination faces the specimen arms have a curved shape in the x–y plane. To ensure the position of rollers A and B along the thickness of the specimen, they were substituted by grub screws, which can be adjusted by using a screwdriver. This is an essential modification compared to the original MSCB configuration [9–12]. This tool is able to produce a nearly pure mode-III fracture (98% mode-III). The details of how to ensure the moment equilibrium of the system is discussed in [32]. For the analysis of the $PSCB_{I/III}$ configuration we superimpose the solutions of the DCB and MSCB specimens. In some recent works [32,33] the IBT solutions for the DCB and MSCB specimens were presented.

3. Analysis

Referring to a previous work [33] the compliance (defined as the crack opening displacement (COD) divided by the applied load) of the DCB specimen at the point of load application (see Fig. 1b) in the x–y plane is:

$$C_{DCB} = \frac{8a^3}{bh^3E_{11}} + \frac{2a^3}{bh^3E_{11}}\left(f_{W1} + f_T + \frac{f_{SV}}{2}\right), \tag{1}$$

where a is the crack length, b is the specimen width, h is the half thickness, E_{11} is the flexural modulus of the specimen, furthermore, f_{W1} is from the Winkler-Pasternak foundation, f_T is from transverse shear and f_{SV} accounts for the Saint–Venant effect:

$$f_{W1} = 5.07\left(\frac{h}{a}\right)\left(\frac{E_{11}}{E_{22}}\right)^{\frac{1}{4}} + 8.58\left(\frac{h}{a}\right)^2\left(\frac{E_{11}}{E_{22}}\right)^{\frac{1}{2}} + 2.08\left(\frac{h}{a}\right)^3\left(\frac{E_{11}}{E_{22}}\right)^{\frac{3}{4}}, \tag{2}$$

$$f_T = \frac{1}{k}\left(\frac{h}{a}\right)^2\left(\frac{E_{11}}{G_{12}}\right), \tag{3}$$

$$f_{SV} = \frac{12}{\pi}\left(\frac{h}{a}\right)\left(\frac{E_{11}}{G_{12}}\right)^{\frac{1}{2}}, \tag{4}$$

where E_{22} is the transverse modulus in the y direction, G_{12} is the shear modulus of the material in the x–y plane and $k = 5/6$ is the

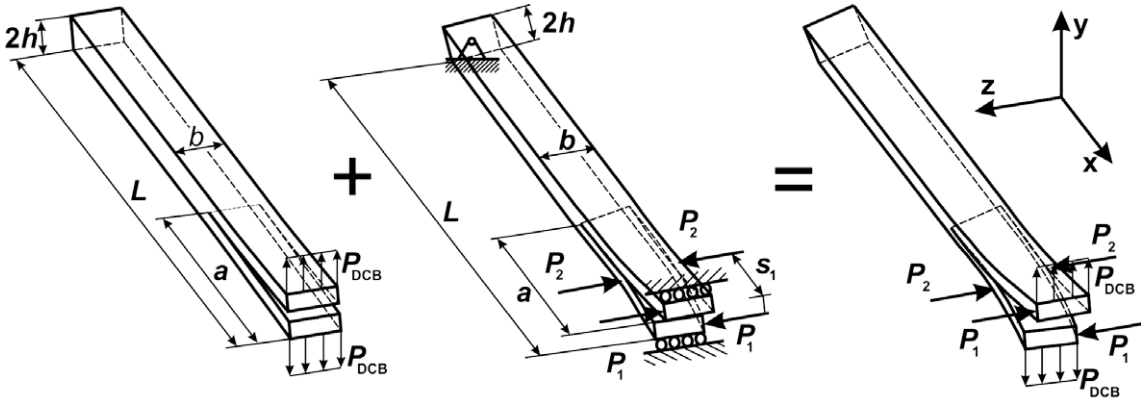

(a) DCB specimen, mode-I (b) MSCB specimen, mode-III (c) $PSCB_{I/III}$ specimen, mixed-mode I/III

Fig. 1. The mixed-mode I/III PSCB specimen (c) as the superposition of the DCB (a) and MSCB (b) specimens.

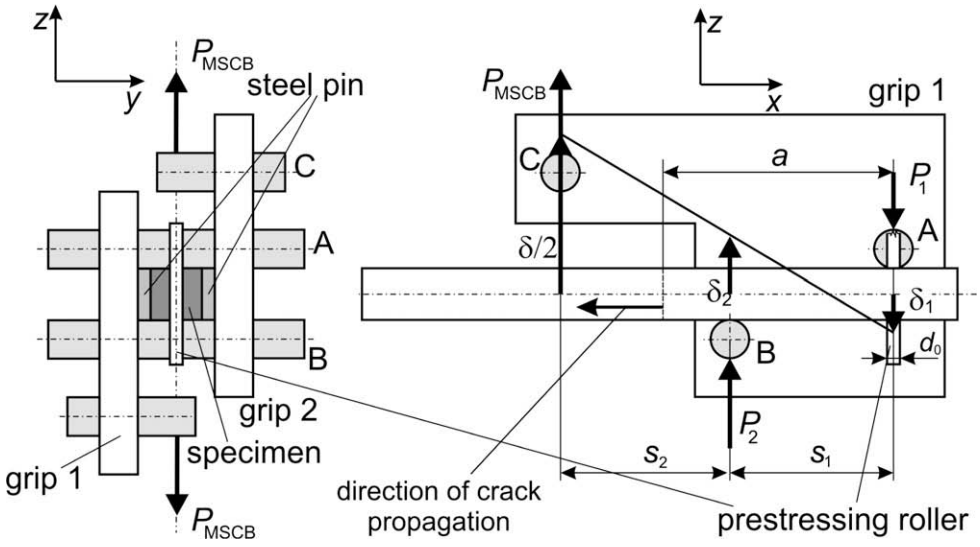

Fig. 2. 2D view of the Prestressed Modified-Split-Cantilever Beam ($PSCB_{I/III}$) specimen.

shear correction factor. The mode-I ERR of the DCB specimen can be obtained by using the Irwin–Kies expression [1]:

$$G_C = \frac{P^2}{2b}\frac{dC}{da}, \tag{5}$$

i.e.

$$G_I = \frac{P_{DCB}^2 a^2 (12 + f_{W2} + f_T + f_{SV})}{b^2 h^3 E_{11}}, \tag{6}$$

where P_{DCB} is the external load, and

$$f_{W2} = 10.14\left(\frac{h}{a}\right)\left(\frac{E_{11}}{E_{22}}\right)^{\frac{1}{4}} + 8.58\left(\frac{h}{a}\right)^2\left(\frac{E_{11}}{E_{22}}\right)^{\frac{1}{2}}. \tag{7}$$

The COD (δ_{DCB}) of the specimen can be controlled by inserting a steel roller between the specimen arms. A reasonable assumption is that the COD is approximately equal to d_0. For this reason we express the force which arises in the DCB specimen by using Eq. (1) and the definition of $C_{DCB} = \delta_{DCB}/P_{DCB}$:

$$P_{DCB} = \frac{bh^3 E_{11} d_0}{8a^3}\frac{1}{1 + (f_{W1} + f_T + f_{SV}/2)/4}, \tag{8}$$

where $d_0 = \delta_{DCB}$ is the diameter of the prestressing roller. Substituting Eq. (8) into Eq. (6) we obtain:

$$G_I = \frac{h^3 E_{11} d_0^2}{64a^4}\frac{[12 + f_{W2} + f_T + f_{SV}]}{[1 + (f_{W1} + f_T + f_{SV}/2)/4]^2}. \tag{9}$$

The analysis of the MSCB specimen is detailed in [32]. The improved model takes four mechanical deformations into account: bending and shearing of the specimen arms, the Saint–Venant effect at the crack front and the free torsion effect in the delaminated portion. The compliance and the ERR calculated by the analytical solution were compared to the results of a three-dimensional finite element model and an excellent agreement was found. Since the MSCB specimen is loaded at four points it should be mentioned that the compliance is calculated at the point of external load application, i.e. at roller C in Fig. 2, the compliance can be measured only at this point. The compliance of the MSCB specimen is:

$$C_{MSCB} = \frac{8a^3}{b^3 h E_{11}}[f_{EB1} + f_{TIM1} + f_{FT1} + f_{S-V1}]. \tag{10}$$

where the terms in the brackets consider bending, transverse shear, free torsion and Saint–Venant effect in the MSCB specimen:

$$f_{EB1} = 1 - 3\left(\frac{s_1 + s_2}{a}\right) + 3\left(\frac{s_1 + s_2}{a}\right)^2 - \frac{s_1(s_1 + s_2)(s_1 + 2s_2)}{a^3}, \tag{11}$$

$$f_{TIM1} = 0.3\left(1 - \frac{s_2^2 - s_1^2}{as_1}\right)\left(\frac{b}{a}\right)^2\left(\frac{E_{11}}{G_{13}}\right), \tag{12}$$

$$f_{FT1} = 0.19\frac{1}{\varsigma}\left(1 - \frac{s_1}{a}\right)\left(\frac{b}{a}\right)^2\left(\frac{E_{11}}{G_{12}}\right), \tag{13}$$

$$f_{S-V1} = 0.48\left(\frac{a - (s_1 + s_2)}{a}\right)^2\left(\frac{b}{a}\right)\left(\frac{E_{11}}{G_{13}}\right)^{\frac{1}{2}}, \tag{14}$$

and

$$\varsigma = 1 - 0.63\mu\frac{h}{b}, \quad \mu = \left(\frac{G_{13}}{G_{12}}\right)^{\frac{1}{2}}, \tag{15}$$

where G_{12} is the shear modulus in the x–y plane, s_1 and s_2 are the distances between the loading rollers A, B and C, respectively (see Fig. 2). Based on Eq. (5) the ERR is given by:

$$G_{III} = \frac{12P_{MSCB}^2 a^2}{b^4 h E_{11}}[f_{EB2} + f_{TIM2} + f_{FT2} + f_{S-V2}], \tag{16}$$

where P_{MSCB} is the applied load of the MSCB specimen, furthermore:

$$f_{EB2} = 1 - 2\left(\frac{s_1 + s_2}{a}\right) + \left(\frac{s_1 + s_2}{a}\right)^2, \tag{17}$$

$$f_{TIM2} = 0.1\left(\frac{b}{a}\right)^2\left(\frac{E_{11}}{G_{13}}\right), \tag{18}$$

$$f_{FT2} = 0.06\frac{1}{\varsigma}\left(\frac{b}{a}\right)^2\left(\frac{E_{11}}{G_{12}}\right), \tag{19}$$

$$f_{S-V2} = 0.32\left(1 - \frac{s_1 + s_2}{a}\right)\left(\frac{b}{a}\right)\left(\frac{E_{11}}{G_{13}}\right)^{\frac{1}{2}}, \tag{20}$$

where G_{13} is the shear modulus in the x–z plane. The condition of at least a 96% mode-III dominant test is [32]:

$$1.02 \le a/(s_1 + s_2) \le 1.09. \tag{21}$$

Combining Eq. (9) with (16) the mode ratio of the $PSCB_{I/III}$ specimen becomes:

$$\frac{G_{III}}{G_I} = \frac{768a^6}{b^4h^4E_{11}^2}\left(\frac{P_{MSCB}}{d_0}\right)^2 f_{I/III}, \tag{22}$$

where

$$f_{I/III} = \frac{[1+(f_{W1}+f_T+f_{SV}/2)/4]^2}{[12+f_{W2}+f_T+f_{SV}]}(f_{EB2}+f_{TIM2}+f_{FT2}+f_{S-V2}), \tag{23}$$

All of the factors in Eq. (23) have been given before. The accuracy of the analytical solution has already been proved in previous papers [32,33]. However, some other questions should be clarified and these are detailed in the followings.

The dependence of the mode ratio on the crack length can be investigated based on Eq. (22). In Table 1 we calculated the mode ratio at $a = 105$ mm using the following material properties: $E_{11} = 33$ GPa, $E_{33} = 7.2$ GPa, and $G_{12} = G_{13} = 3$ GPa. The geometrical properties are: $b = 12.5$ mm, $2h = 6.2$ mm, $s_1 = 49.26$ mm, $s_2 = 51.15$ mm. In the calculation we increased subsequently the crack length by small increments until 2 mm. If the crack length is measured inaccurately it has a major influence on the mode ratio. If $\Delta a = 1$ mm then the expected error is 10%. So, the accurate measurement of the crack length after crack initiation is important. During the experiments (see later) a transparent material is used, so the crack initiation is easy to be identified. If the material under consideration is non-transparent then the solution is for example the application of ultrasonic or acoustic emission equipment for the identification of the crack initiation.

If the crack opening is relatively large then the crack length will be shorter than its original value. This is due to the fact that the contact point between the specimen arms and the roller is located to a distance of a^* instead of "a" from the crack tip, as it is shown in Fig. 3. We can easily calculate the distance, a^* based on a simple geometrical analysis. For clarity, in Fig. 3 we need to find the coordinate, a^* where the derivative of $f_1(x)=(d_0/2)^2\cdot(x/a)^3$ (simple beam theory solution) and $f_2(x)=((d_0/2)^2-(x-a)^2)^{1/2}$ (equation of a circle with diameter, d_0) is the same. Table 2 shows the changes of the crack length, and the difference compared to the original crack length. In the worst case (if $d_0 = 13$ mm) we make a mistake of 1% considering the crack length. A reasonable conclusion is that the shortening of the crack length is negligible.

In a recently published work it was shown that the torque of the MSCB specimen depends on the distance between the neutral planes of the specimen arms [32]. If we insert a steel roller, then the neutral planes become curved and the distance between them also increases along the x axis. Theoretically we would expect higher torque in the specimen arms in this case. To clarify this question a finite element analysis was performed. For the calculation the COSMOS/M 2.6 package was used. The elastic properties of the models were: $E_{11} = 33$ GPa, $E_{22} = E_{33} = 7.2$ GPa, $G_{12} = G_{13} = G_{23} = 3$ GPa and $\nu_{12} = \nu_{13} = \nu_{23} = 0.27$. The geometrical properties are: $b = 12.5$ mm, $2h = 6.2$ mm, $s_1 = 49.26$ mm, $s_2 = 51.15$ mm and the length of the models was $L = 150$ mm (refer to Fig. 1). The three-dimensional model of the MSCB specimen was built using linear eight-node SOLID brick elements. The imposed boundary conditions and the loading of the model are demonstrated in Fig. 4a. On the one hand the model was loaded at the end of the specimen

Table 1
The changes in the mode ratio G_{III}/G_I in the case of inaccurate crack initiation detection if $a = 105$ mm.

Δa	0.25	0.35	0.5	0.75	1	1.25	1.5	2
Difference (%)[a]	2.42	3.41	4.91	7.47	10.1	12.79	15.56	21.33

[a] $(G_{III}/G_I|_{a+\Delta a}-G_{III}/G_I|_{a=105})/(G_{III}/G_I|_{a=105})$.

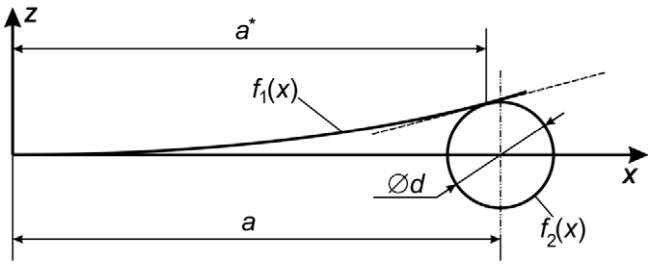

Fig. 3. The effect of the prestressing roller on the crack length of the $PSCB_{I/III}$ specimen.

arm by a displacement value equal to half of the diameter of the steel rollers ($d_0 = 6$, 7, 8, 10, 12 and 13 mm) providing the mode-I part of the mixed-mode I/III ERR. On the other hand the model was also loaded in-planes parallel to the delamination (from $h/2$ distance to the specimen side) using the load values (P_1 and P_2) which were calculated using $P_{MSCB} = 200$ N ($P_1 = P_{MSCB}\cdot s_2/s_1$ and $P_2 = P_{MSCB}\cdot(1+s_2/s_1)$). The results obtained are summarized in Table 3, which show that in all of the cases we obtained the same displacements and angle of twists. So, the finite element analysis shows that the torque, the displacements at rollers A and B and the angle of twists (denoted by φ in Fig. 4a) are independent of the crack opening. This will be confirmed also by experiments (see later). From other point of view the superposition of the analytical solutions for the DCB and MSCB specimens is reasonable.

A major question in a mixed-mode configuration is how the mode ratio changes along the crack front, and how much is its effect on the ERRs. To clarify this question the same finite element model as shown in Fig. 4b, is utilized. In the crack tip a refined mesh was constructed and the mode-I, mode-II and mode-III ERRs were evaluated by using the virtual crack-closure technique (VCCT) [34], the size of the crack tip elements were $\Delta x = \Delta y = 0.25$ mm and $\Delta z = 0.78125$ mm (refer to Fig. 4 for the coordinate system).

Figs. 5a, b and 6a show the distribution of the ERRs along the crack front in the case of $d_0 = 6$, 8 and 13 mm, while Fig. 6b shows the variation of the mode ratio in each case. The values of P_{MSCB} were determined based on crack initiation experiments (see later). As it can be seen even the mode-I, mode-II and mode-III ERRs have a symmetric distribution along the crack front. It is also important to note that the mode-II component can not be eliminated entirely, it is about 2–6% of the total ERR. In Figs. 5a, b and in Figs. 6a, b, the average ERRs and mode ratios were obtained by dividing the integrated area under the curve by the specimen width. Table 4 shows the comparison of the IBT to the VCCT with respect to the average ERR and mode ratio. The IBT overestimates G_I at most with 2.2% and underestimates G_{III} at most with 6.5%. This results in a maximum difference of −8.4% in the mode ratio. Overall this agreement is quite good and based on these results the IBT scheme is a possible data reduction scheme for the $PSCB_{I/III}$ test.

Since the ERR varies along the crack front, i.e. it is highest at the center and lowest at the specimen edges it is obvious that the specimen possess a curved crack front under crack propagation. So, as it is seen in Fig. 6b, a constant mode ratio along the crack front is not possible to be produced. Consequently, some assumptions are required considering the reduction of the experimental data. In the data reduction and the calculation of G and G_{III}/G_I the widthwise average values will be adopted. To assess the possible errors (shown in Figs. 5a, b and 6a) in the calculation of G and G_{III}/G_I by the IBT we assume that the crack initiation takes place at the point where the total ERR (G_T) reaches the highest value. These points are indicated in Figs. 5a, b and 6a, b and the location of these points from the left specimen side is denoted by z_{max}. In Table 4 the ERRs

Table 2
The changes in the crack length of the prestressed specimen with the steel roller diameter.

d_0 (mm)	0	6	7	8	10	12	13
a^* (mm)	105.00	104.74	104.65	104.55	104.30	104.01	103.84
Difference compared to a = 105 mm (%)	0.00	0.25	0.33	0.43	0.67	0.95	1.10

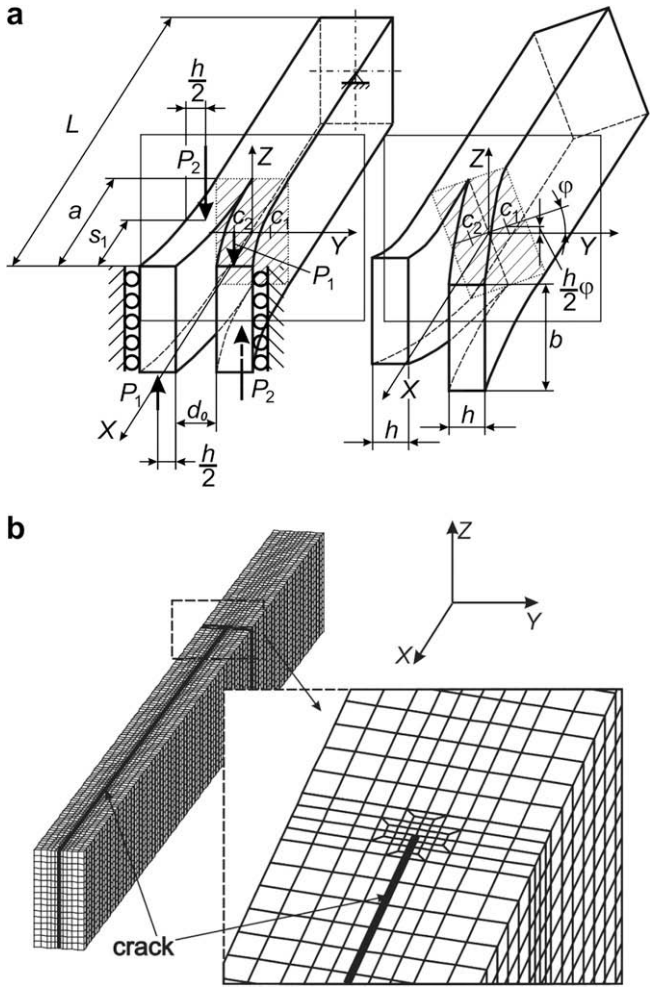

Fig. 4. The applied boundary conditions of the $PSCB_{I/III}$ specimen (a) and the details of the FE model (b).

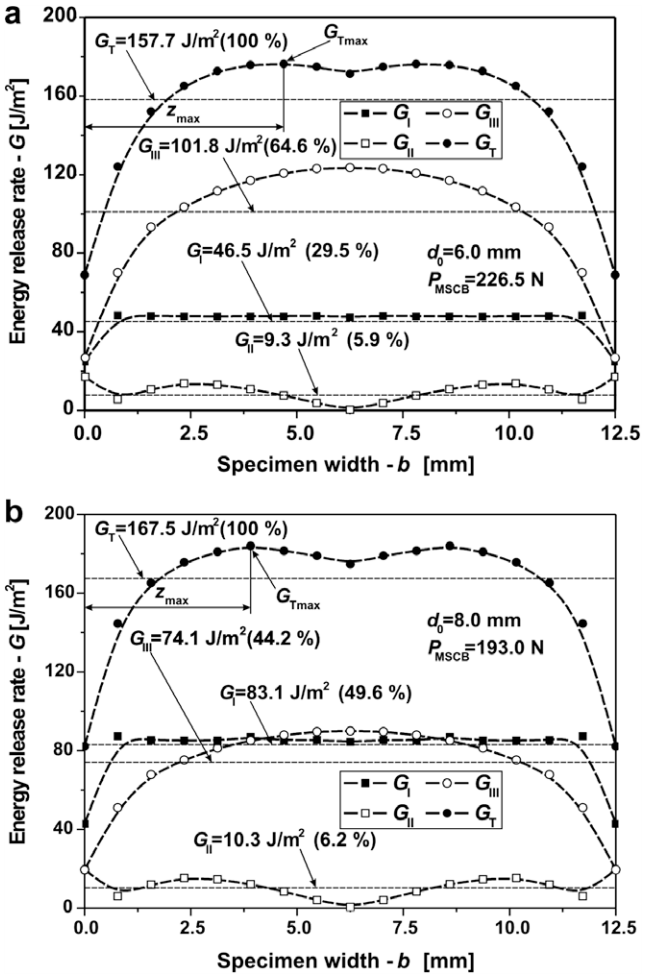

Fig. 5. The distribution of the mode-I, mode-II and mode-III ERRs along the crack front in the case of d_0 = 6 mm (a) and d_0 = 8 mm (b).

Table 3
The effect of the steel roller on the displacements and angle of twist of the $PSCB_{I/III}$ specimen.

d_0 (mm)	0	6	7	8	10	12	13
δ_A ($x = a$, z = 6.25, y = 1.55) (mm)	1.2545	1.2545	1.2545	1.2545	1.2545	1.2545	1.2545
δ_B ($x = a-s_1$, z = 6.25, y = 1.55) (mm)	0.05355	0.05356	0.05356	0.05356	0.05356	0.05356	0.05356
φ_c ($x = c$) (°)	5.9781	5.9786	5.9786	5.9786	5.9786	5.9786	5.9786
φ_0 (x = 0) (°)	5.8656	5.8652	5.8652	5.8652	5.8652	5.8652	5.8652

δ_A – displacement at roller A.
δ_B – displacement at roller B.
φ_c – angle of twist at the end of the specimen.
φ_0 – angle of twist at the crack tip of the specimen.

and mode ratios are calculated by using the values by VCCT at z_{max} too and they compared to the result of IBT. The difference in G_I is negligible. On the contrary, in the worst case the value of G_{III} at z_{max} is 20.8% higher than that by the IBT. Although the difference subsequently decreases to 14.7%, it seems to be significant. The difference in the mode ratio is 20.2% if d_0 = 6.0 mm and it also decays to 13.4%. In accordance with Table 4 the higher the diameter of the steel roller is the closer z_{max} to left side of the specimen is.

Although the possible errors in the analytically obtained mode ratio is relatively high, we prefer the IBT as a data reduction scheme, because the finite element analysis based data reduction requires much computational time. Moreover, assumption is also

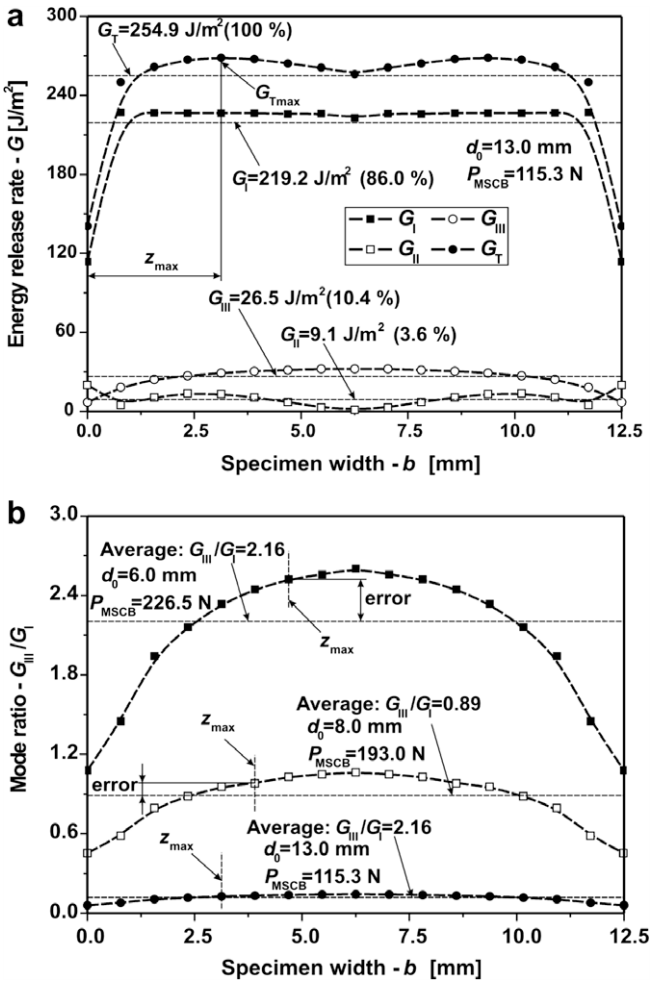

Fig. 6. The distribution of the mode-I, mode-II and mode-III ERRs along the crack front in the case of d_0 = 13 mm (a) and the variation of the mode ratio along the crack front if d_0 = 6, 8 and 13 mm (b).

required if we apply the VCCT to reduce the experimental data, and the IBT agrees excellently with the widthwise average G and G_{III}/G_I. It should be mentioned that a similar variation of the mode ratio exist in the 8PBP system too [28], wherein the authors defined a zone based on the 90% of the total ERR and crack initiation was expected within this zone. An advantage of the $PSCB_{I/III}$ over the 8PBP test is that an analytical reduction technique exists.

In the sequel the details of the experimental work is presented.

4. Experiments

4.1. Material properties

The constituent materials of the E-glass/polyester composite were procured from Novia Ltd. The properties of the E-glass fiber are E = 70 GPa and ν = 0.27, and the properties of the unsaturated polyester resin we applied are: E = 3.5 GPa and ν = 0.35. Both were considered to be isotropic. The unidirectional $([0°]_{14})$ E-glass/polyester specimens with thickness of $2h$ = 6.2 mm, width of b = 12.5 mm, and fiber-volume fraction of V_f = 43% were manufactured in a special pressure tool. A polyamide (PA) insert with thickness of 0.03 mm was placed at the midplane of the specimens to make an artificial starting defect. It should be highlighted that this film thickness is higher than the 0.013 mm recommended in the DCB and MMB test standards [2,3].

A great advantage of the present E-glass/polyester material is the transparency, which makes it possible to observe the crack initiation visually. The tool was left at room temperature until the specimens became dry. Then the specimens were removed from the tool and were further left at room temperature until 4–6 h. The specimens were cut to the desired length and were precracked in opening mode of 4–5 mm by using a sharp blade.

The flexural modulus of the material was determined from a three-point bending test with span length of $2L$ = 150 mm using six uncracked specimens with thickness of $2h$ = 6.2 mm and width of b = 20 mm. The flexural modulus was computed in accordance with simple beam theory expression: $\delta_{bend} = PL^3/(4bh^3E_{11})$, which is the displacement at the point of load introduction. The experiments resulted in E_{11} = 33 GPa. In fact the shear deformation was not accounted for, however its contribution to the displacement is very small: $\delta_{shear} = PL/(4bhkG_{12})$. The additional properties were predicted from simple rules of mixture, in this way $E_{22} = E_{33}$ = 7.2 GPa, $G_{12} = G_{13}$ = 3 GPa and $\nu_{12} = \nu_{13}$ = 0.27 were obtained. Using these values the ratio of the displacements from bending and shear deformation at the center of the specimens is: $(h/L)^2 \cdot E_{11}/(G_{12}k)$ = 0.0056, i.e. the amount of shear deformation is very small and can be neglected. To confirm the assumption that the material is transversely isotropic the specimens were cut along the longitudinal direction in order to obtain very narrow

Table 4
Comparison of the ERRs and mode ratios by beam and finite element analysis.

Roller diameter	d_0 (mm)	0 (MSCB)	6	7	8	10	12	13	~15 (DCB)
Load at crack initiation	P_{MSCB} (N)	247.8	226.50	214.00	193.00	171.60	133.00	115.30	0
G_I (J/m²)	IBT[a]	–	47.5	64.7	84.5	132.1	190.2	223.2	412
	VCCT widthwise av.[b]	–	46.5	63.3	83.1	130.2	186.1	219.2	–
	VCCT at z_{max}[c]	–	47.9	65.9	86.8	135.2	191.9	226.6	–
	Difference (a-b)/b (%)	–	2.20	2.24	1.77	1.40	2.19	1.80	–
	Difference (a–c)/c (%)	–	−0.77	−1.82	−2.67	−2.33	−0.89	−1.49	–
G_{III} (J/m²)	IBT [a]	114.5	95.6	85.3	69.5	54.9	33.0	24.8	–
	VCCT widthwise av.[b]	121.9	101.8	90.9	74.1	58.6	35.2	26.5	–
	VCCT at z_{max}[c]	–	120.8	104.5	85.2	64.3	38.6	29.1	–
	Difference (a-b)/b (%)	−6.05	−6.10	−6.13	−6.29	−6.28	−6.34	−6.47	–
	Difference (a–c)/c (%)	–	−20.83	−18.31	−18.45	−14.56	−14.61	−14.71	–
G_{III}/G_I	IBT[a]	∞	2.01	1.32	0.82	0.42	0.17	0.11	0
	VCCT widthwise av.[b]	∞	2.19	1.44	0.89	0.45	0.19	0.12	–
	VCCT at z_{max}[c]	∞	2.52	1.58	0.98	0.48	0.20	0.13	–
	Difference (a-b)/b (%)	–	−8.11	−8.19	−7.92	−7.57	−8.35	−8.12	–
	Difference (a–c)/c (%)	–	−20.22	−16.79	−16.21	−12.52	−13.84	−13.42	–

[a] Improved beam theory.
[b,c] Virtual Crack-Closure Technique.

specimens. The narrow specimens were rotated by 90° about the longitudinal axis compared to the original measurements and the slope of the load–displacement data of the specimens was measured again. These experiments resulted also in $E_{11} = 33$ GPa, i.e. the material was found to be transversely isotropic. The material properties were used in the data reduction process.

4.2. Double-cantilever beam test

In the case of the DCB test (Fig. 1b) we refer to previous fracture experiments [35] performed in the crack length range of $a = 20$ to 150 mm. It has been found that the initiation critical ERR becomes independent of a, after 90 mm. The steady-state ERR was $G_{IC} = 412$ J/m^2 evaluated by using an IBT scheme. This value will be used in the sequel.

4.3. Modified split-cantilever beam test

For the MSCB measurements four specimens were prepared with $a = 105$ mm and $s_1 = 49.26$ mm and $s_2 = 51.15$ mm, respectively. Each specimen was put into the loading rig shown in Fig. 7, the rig was adjusted in order to eliminate any play of the specimens. Then the specimens were loaded, the load and displacement values were read from the scale of the testing machine and using a mechanical dial gauge. The crack initiation was identified visually, so when the first non-uniformity in the previously straight crack front was observed it was believed to be the point of crack initiation.

4.4. Prestressed split-cantilever beam test

The experimental equipment for the PSCB$_{I/III}$ test is demonstrated in Fig. 7. The tests were carried out using an Amsler testing machine under displacement control. The crack length of interest was $a = 105$ mm. The critical crack opening displacement measured from the DCB test [35] is about 15 mm (if $a = 105$ mm). Six steel rollers were used including the following diameters: $d_0 = 6$, 7, 8, 10, 12 and 13 mm. It was assumed that the crack opening displacements (δ_{DCB}) were identical to these values. The specimen arms transmitted a relatively high pressure to the steel roller, therefore the position of the rollers was always stable and no slip along the x axis was observed during the measurements. Similarly to the MSCB tests, we applied four coupons at each steel roller. The load–deflection data was measured by using the scale of the testing machine and a mechanical dial gauge (see Fig. 7). In each case the critical load at crack initiation was determined.

5. Results and discussion

It will be shown subsequently that the stiffness, the compliance and the mode-III ERR of the PSCB$_{I/III}$ specimen are identical (with a very good approximation) to those of the MSCB specimen.

5.1. Load and displacement

Fig. 8a shows a recorded load–displacement curve for the PSCB$_{I/III}$ specimen if $d_0 = 8.0$ mm. The response follows essentially a linear relation. The PSCB$_{I/III}$ test was performed according to the followings. The onset of crack advance was identified by visual observations. In each case four specimens were tested, one of them was used to investigate the crack front. The other three specimens were loaded continuously and the crack initiation was observed in situ. So, the former specimen was loaded subsequently, at some points, where the initiation was expected the specimen was relieved, removed from the rig and the crack front was photographed. When the first non-uniformity was observed, then this point was denoted to be the point of fracture initiation. The results of this process are demonstrated in Fig. 8b, for the PSCB$_{I/III}$ system at a prestressed state with $d_0 = 8.0$ mm.

Table 5 shows that the slopes of the load–displacement traces of the MSCB ($d_0 = 0$) and PSCB$_{I/III}$ specimens are eventually the same, consequently the prestressed state does not influence noticeably the stiffness of the system and the compliance of the PSCB$_{I/III}$ can be assumed to be equal to that of the MSCB system. The maximum difference is 10.5% between the measured and calculated slopes. On the other hand the results in Table 5, confirm that the effect of friction between the steel roller and the specimen arms on the load–displacement response of the system is insignificant.

5.2. Data reduction

Two reduction techniques (IBT and DBT) were applied to reduce the experimental data. In a relevant work [31] for the mixed-mode I/II version of the PENF specimen four reduction schemes were

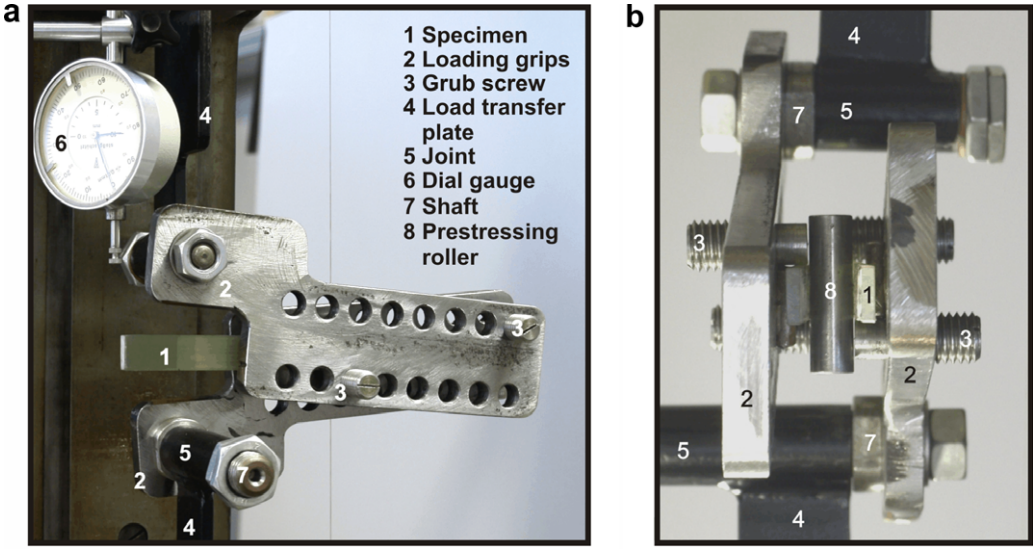

Fig. 7. The experimental equipment of the PSCB$_{I/III}$ specimen. Side view (a) and front view (b).

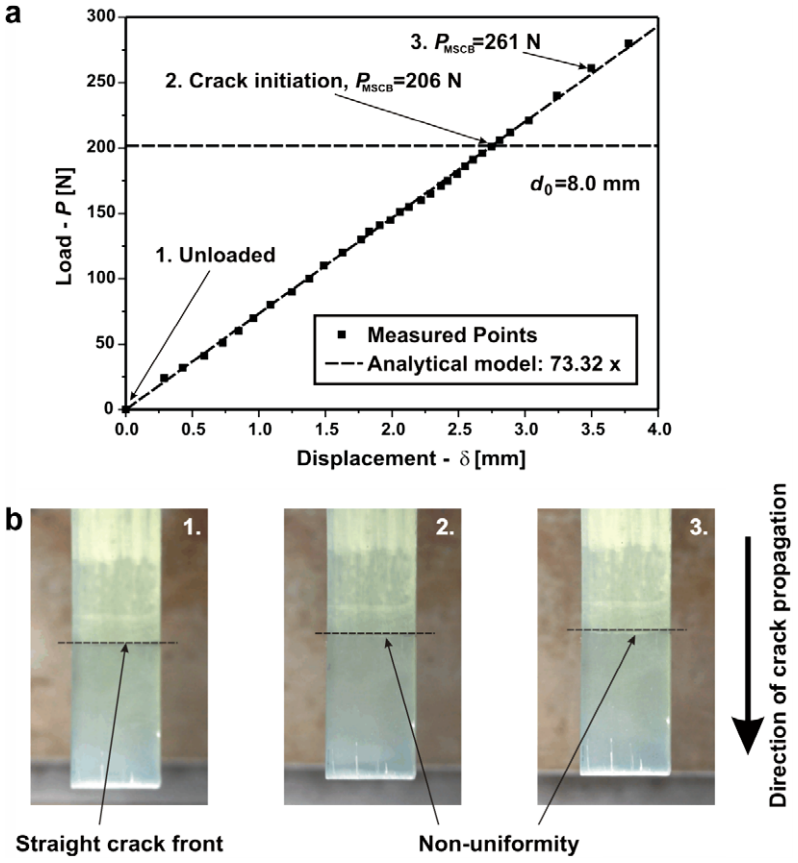

Fig. 8. Load–displacement curve of the $PSCB_{I/III}$ system if d_0 = 8.0 mm (a). The identification of crack initiation during the fracture process (b).

Table 5
The changes in the slope of the load displacement curves of the $PSCB_{I/III}$ specimen with the roller diameter.

d_0 (mm)	0	6	7	8	10	12	13
Load–displacement curve slope-1 (N/mm)	77.429	75.041	81.007	72.662	75.411	76.561	77.583
Difference compared to 73.32 N/mm[a]	5.60	2.35	10.48	−0.90	2.85	4.42	5.81
Load–displacement curve slope-2 (N/mm)	75.736	75.828	76.155	73.153	80.714	78.663	78.289
Difference compared to 73.32 N/mm[a]	3.30	3.42	3.87	−0.23	10.08	7.29	6.78

[a] Result of the analytical model.

utilized: IBT, simple beam theory, DBT, e.g. [36] and the compliance calibration (CC). For mode-I and mode-II specimens the CC is thought to be the most accurate one. From other point of view the CC method is unreliable for the MSCB due to certain reasons discussed by Cicci et al. [9] and Szekrényes [30]. For the $PENF_{II/III}$ system the data reduction techniques applied were: IBT, CC and the FEM, respectively [30]. It has been shown that the optimal solution is the application of IBT, however this is mainly due to the relatively small compliance values measured in the MSCB specimen and the complexity of the finite element data reduction.

5.2.1. Improved beam theory

5.2.1.1. Double-cantilever beam. In Eq. (6) P_{DCB} should be replaced with P_I (the load value at crack initiation in the DCB specimen) in order to obtain the improved analytical expression for the ERR of the DCB specimen (G_{IC} = 412 J/m^2 from IBT [35]).

5.2.1.2. Modified split-cantilever beam specimen. Replacing P_{MSCB} with P_{III} in Eq. (16) gives the improved solution for the MSCB coupon, where P_{III} is the critical load value at crack onset. The IBT resulted in G_{IIIC} = 114.5 ± 16.0 J/m^2.

5.2.1.3. Prestressed split-cantilever beam specimen. The improved analytical solutions are given by Eqs. (9) and (16) for the $PSCB_{I/III}$ system.

It should be emphasized that in general the additional material properties (E_{22}, G_{12}, G_{13}) of the composite are not known with the desired accuracy. The reason for that is the different rules of mixture give only approximate results. Hence the results of the improved expressions should be used carefully.

5.2.2. Direct beam theory

5.2.2.1. Double-cantilever beam. For the DCB specimen we replace the result of DBT with the one by IBT (G_{IC} = 412 J/m^2).

5.2.2.2. Modified split-cantilever beam specimen. In accordance with DBT it is possible to obtain the following scheme for the MSCB specimen [36]:

$$G_{DBT} = \frac{3P_{III}\delta_{MSCB}}{2ba}\left(\frac{f_{EB2}+f_{TIM2}+f_{FT2}+f_{S-V2}}{f_{EB1}+f_{TIM1}+f_{FT1}+f_{S-V1}}\right), \tag{24}$$

where the coefficients in the parentheses are given by Eqs. (11)–(15), (17)–(20). In Eq. (14) P_{III} and δ_{MSCB} are the experimentally measured

load and displacement values at the point of crack initiation in the MSCB specimen.

5.2.2.3. Prestressed split-cantilever beam specimen. We obtain the DBT scheme for G_{III} the $PSCB_{I/III}$ system if we replace P_{III} with P_{MSCB} in Eq. (24) (G_I is calculated by IBT).

The application of DBT requires also the knowledge of additional material properties (E_{22}, G_{12}, G_{13}) of the composite material.

5.3. Critical energy release rates

The critical mode-I, mode-III and the mixed-mode I/III ERRs at crack initiation and the mode mix calculated by the IBT are given in Table 4. The geometries tested had properties of $a = 105$ mm, $2h = 6.2$ mm, $s_1 = 49.26$ mm, $s_2 = 51.15$ mm and $L = 150$ mm and at each value of the diameter of the prestressing roller (d_0) four coupons were used. Table 6 presents the results obtained by the DBT scheme. In fact the scatter of the mode-I ERR component is zero, this is because the mode-I ERR is provided by the preload of the specimen. Otherwise, the mode-I components were substituted by the results of the IBT scheme. Comparing Tables 4 and 6 the difference between the G_{III} values – as well as the mode ratio – by DBT and IBT decreases with the roller diameter (which is eventually the COD).

It is important to recommend a data reduction technique for the $PSCB_{I/III}$ system. The reliability and simplicity of the IBT has already been highlighted by other authors (e.g. [24,37]), On the other hand the application of the FEM as a data reduction method requires large computational time. From other perspectives the DBT method is inaccurate if the mode-I component is small. So, it is straightforward that at the present stage the optimal solution is the application of IBT for the evaluation of both the mode-I and mode-III ERRs, however the theoretically possible errors should be considered (see Section 3 and Table 4). Obviously, giving lower G_{III} values the IBT is more conservative than the VCCT.

It is also possible that the additional material properties (E_{22}, E_{33}, G_{12}, G_{13}, ν_{12}, ν_{13}) are determined inaccurately. In a recent work the mixed-mode I/II and II/III versions of the PENF were presented and experiments were performed for the same E-glass/polyester material [30,31]. The results of the IBT technique were compared to that of the CC method leading to a very good agreement between them. It is well-known that the CC method is reliable for the data reduction in common mode-I and mode-II tests. So, it may be assumed that the additional material properties were determined with an efficient accuracy for the $PENF_{I/II}$ and $PENF_{II/III}$ systems and they can be utilized also for the $PSCB_{I/III}$ system.

5.4. Fracture envelopes

In order to construct a fracture envelope in the G_I–G_{III} plane we apply the two most popular criteria, which are frequently used in studies related to fracture characterization of composite materials under mixed-mode I/II condition. It is assumed that they can be applied also for mixed-mode I/III fracture. It is a reasonable assumption that the small mode-II component (refer to Figs. 5 and 6) does not influence significantly the fracture envelope. In accordance with the traditional power criterion the following relation may be established between the mode-I and mode-III ERRs [37]:

$$\left(\frac{G_I}{G_{IC}}\right)^{p_1} + \left(\frac{G_{III}}{G_{IIIC}}\right)^{p_2} = 1. \tag{25}$$

Williams' criterion [38] recommends the following expression for the relation between the mode-I and mode-III ERRs:

$$\left(\frac{G_I}{G_{IC}} - 1\right)\left(\frac{G_{III}}{G_{IIIC}} - 1\right) - I_i\left(\frac{G_I}{G_{IC}}\right)\left(\frac{G_{III}}{G_{IIIC}}\right) = 0, \tag{26}$$

where I_i is the interaction parameter between the mode-I and mode-III ERRs. If $I_i = 0$ then there is no interaction. Also, if $I_i = 1$ then Eq. (26) states a simple addition. In Eqs. (25) and (26) G_{IC} is the critical ERR under pure mode-I (calculated from the data of the DCB specimen), G_{IIIC} is the mode-III critical ERR (calculated from the data of the MSCB specimen). The results of the $PSCB_{I/III}$ test listed in Table 4 (IBT) were used to provide six additional points in the G_I–G_{III} plane. The power parameters (p_1, p_2) in Eq. (25) and the interaction parameter (I_i) in Eq. (26) were determined by a curve-fit technique by applying the ORIGINPRO 7.0 code.

The fracture envelope calculated by the IBT method is displayed in Fig. 9. The main conclusion is that there is some interaction between the mode-I and mode-III ERRs, although the relation between G_I and G_{III} is almost linear. The scatter is also in reasonable ranges and it decreases with the increase of G_{IC}. Overall, the difference between the power and Williams' criteria is negligible; both describe the same failure locus. We point out again that in each point (except in that of the DCB) there is a small mode-II contribution to the ERR. Therefore, it is assumed that the determined envelope is very close to that, when there were no mode-II contribution.

In two recent works the fracture envelopes in the G_I–G_{II} and G_{II}–G_{III} planes were constructed by the mixed-mode I/II and II/III version of the PENF specimen ($PENF_{I/II}$ and $PENF_{II/III}$) for the same E-glass/polyester material [30,31]. A similar experimental study resulted in a concave envelope in the G_I–G_{II} and a convex one in the G_{II}–G_{III} plane as it is shown in Figs. 10a and b. It is important to note, that the envelopes in Figs. 10a and b, were determined using specimens with $a = 55$ mm, while the present one in Fig. 9, is for the case of $a = 105$ mm. Based on the comparison between Figs. 9 and 10a, b we may conclude that the material behaves differently under mixed-mode I/II and mixed-mode II/III loading conditions, but proves similar behavior in the G_I–G_{II}, and the G_I–G_{III} plane. It is also important to note that interaction takes place in both cases.

6. Conclusions

In this work the mixed-mode I/III version of the prestressed split-cantilever beam specimen was developed for interlaminar fracture testing of laminated transparent composite materials. Apart from the MSCB and the traditional DCB tests the $PSCB_{I/III}$ specimen was used to obtain the mixed-mode I/III energy release

Table 6
Critical energy release rates calculated by DBT.

	d_0 (mm)	0 (MSCB)	6	7	8	10	12	13	~15 (DCB)
Direct beam theory (DBT)	G_{III}/G_I	∞	1.75	1.12	0.73	0.36	0.16	0.10	0.00
		–	±0.19	±0.18	±0.11	±0.04	±0.02	±0.01	–
	G_I (J/m2)	0.0	47.5	64.7	84.5	132.1	190.2	223.2	412.0 (IBT)
	G_{III} (J/m^2)	100.5	83.3	72.7	61.7	47.0	29.7	21.2	0.0
		±16.3	±9.2	±11.4	±9.3	±5.4	±4.2	±1.4	–
	G_T	100.5	130.8	137.4	146.2	179.1	219.8	244.4	412.0 (IBT)

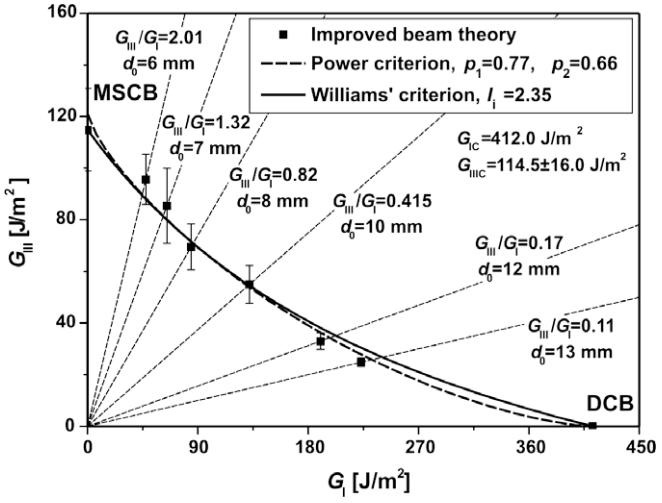

Fig. 9. Interlaminar fracture envelope in the G_I–G_{III} plane for E-glass/polyester composite material calculated by the IBT method.

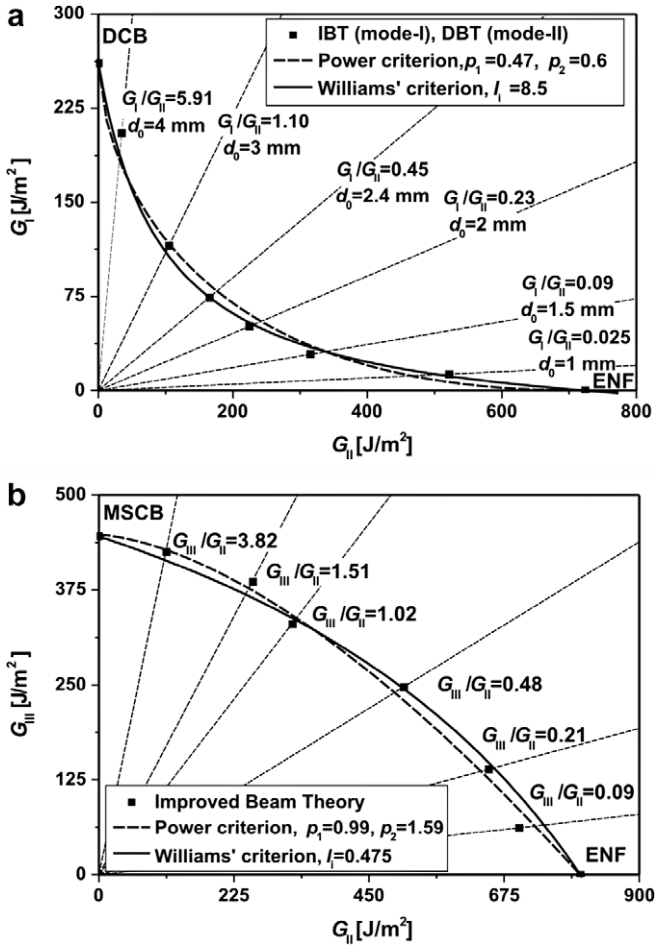

Fig. 10. Interlaminar fracture envelopes in the G_I–G_{II} and the G_{II}–G_{III} planes for E-glass/polyester composite material.

rate at crack propagation onset including six different mode ratios. To perform the experiments unidirectional E-glass/polyester specimens were manufactured. An improved beam model was recommended for the evaluation of both the mode-I and mode-III energy release rate.

A finite element analysis was performed and it was shown that the mode ratio changes along the specimen width and it is not possible to eliminate this variation. The beam theory expressions give a widthwise average value of the energy release rates and mode ratio compared to the finite element results. In this respect some assumptions were made considering the data reduction, namely the widthwise average values were believed to give acceptable and realistic results. To assess the possible errors committed through these assumptions finite element analysis was performed using the virtual crack-closure technique. The crack initiation was expected at the point where the maximum of the total energy release rate was calculated and the values of G_{III} and G_{III}/G_I were compared to the widthwise average values. The possible errors were estimated to be at most 20.8% in G_{III} and 20.2% in G_{III}/G_I, however these differences decrease with the increase of the mode-I component of the energy release rate.

Based on the performed experimental work the fracture envelope of the present material was determined indicating some interaction between G_I and G_{III}.

The $PSCB_{I/III}$ specimen offers several advantages. First of all, it incorporates the traditional beam-like specimen geometry. Second, it was shown that the $PSCB_{I/III}$ specimen is able to produce any mode ratio at crack propagation onset. The drawbacks of the PSCB specimen are the low compliance values; the mode ratio changes with the crack length and the applied load, so the method is recommended mainly for the testing of transparent composite materials. Moreover the mode ratio changes along the crack front. Finally, the mode ratio can not be calculated without performing experiments (i.e. it can not be designated before the test), involving the fact that the mode ratio will depend on the definition of the crack initiation and the accuracy of the measurement of the load and crack length.

More research is needed to reduce the drawbacks of the test and to develop new data reduction schemes.

Acknowledgements

This paper was supported by the János Bolyai Research Scholarship of the Hungarian Academy of Sciences and the National Science and Research Fund (OTKA) under Grant No. T34040. The author is grateful to his father (András L. Szekrényes) for the construction of the experimental equipments.

References

[1] Anderson TL. Fracture mechanics – fundamentals and applications. 3rd ed. Boca Raton, London, New York, Singapore: CRC Press, Taylor & Francis Group; 2005.
[2] Brunner AJ, Flüeler P. Prospects in fracture mechanics of "engineering" laminates. Eng Fract Mech 2005;72:899–908.
[3] Brunner AJ, Blackman BRK, Davies P. A status report on delamination resistance testing of polymer–matrix composites. Eng Fract Mech 2008;75:2779–94.
[4] Donaldson SL. Mode III intelaminar fracture characterization of composite materials. Compos Sci Technol 1988;32:225–49.
[5] Hwang S-F, Hu C-L. Tearing mode interlaminar fracture toughness of composite materials. Polym Compos 2001;22:57–64.
[6] Naik NK, Reddy KS, Meduri S, Raju NB, Prasad PD, Azad SKNM, et al. Interlaminar fracture characterization for plain weave fabric composites. J Mater Sci 2002;37:2983–7.
[7] Becht G, Gillespie Jr JW. Design and analysis of the crack rail shear specimen for mode III interlaminar fracture. Compos Sci Technol 1988;31:143–57.
[8] Robinson P, Song QD. The development of an improved mode III delamination test for composites. Compos Sci Technol 1994;52:217–33.
[9] Cicci D, Sharif F, Kortschot MT. Data reduction for the split cantilever beam mode III delamination test. In: Proceedings, ACCM 10, Whistler, British Columbia, Canada, 14–18 August, 1995.
[10] Sharif F, Kortschot MT, Martin RH. Mode III delamination using a split cantilever beam. In: Martin RH, editor. Composite materials: fatigue and fracture – fifth volume ASTM STP 1230, Philadelphia: ASTM;1995. p. 85–99.
[11] Trakas K, Kortschot MT. The relationship between critical strain energy release rate and fracture mode in multidirectional carbon-fiber/epoxy laminates. In:

Armanios EA, editor. Composite materials: fatigue and fracture – sixth volume ASTM STP 1285, ASTM; 1997. p. 283–304.
[12] Rizov V, Shindo Y, Horiguchi K, Narita F. Mode III interlaminar fracture behaviour of glass fiber reinforced polymer woven laminates at 293 to 4 K. Appl Compos Mater 2006;13:287–304.
[13] Farshad M, Flüeler P. Investigation of mode III fracture toughness using an anti-clastic plate bending method. Eng Fract Mech 1998;60:5–6.
[14] Podczeck F. The determination of fracture mechanics properties of pharmaceutical materials in mode III loading using an anti-clastic plate bending method. Int J Pharm 2001;227:39–46.
[15] Lee SM. An edge crack torsion method for mode III delamination fracture testing. J Compos Technol Res 1993;15(3):193–201.
[16] Liao WC, Sun CT. The determination of mode III fracture toughness in thick composite laminates. Compos Sci Technol 1996;56:489–99.
[17] Suemasu H. An experimental method to measure the mode-III interlaminar fracture toughness of composite materials. Compos Sci Technol 1999;59: 1015–21.
[18] Ratcliffe JG. Characterization of the edge crack torsion (ECT) test for mode III fracture toughness measurement of laminated composites. NASA/Technical Memorandum-2004-213269.
[19] Pennas D, Cantwell WJ, Compston P. The influence of strain rate on the mode III interlaminar fracture of composite materials. J Compos Mater 2007;41: 2595–614.
[20] Morais AB, de Pereira AB, Moura MFSF, de Magalhães AG. Mode III interlaminar fracture of carbon/epoxy laminates using the edge crack torsion (ECT) test. Compos Sci Technol 2009;69:670–6.
[21] Moura MFSF, de Fernandez MVC, Morais AB, de Campilho RDSG. Numerical analysis of the edge crack torsion test for mode III interlaminar fracture of composite laminates. Eng Fract Mech 2008;76(4):469–78.
[22] Ehart RJA, Stanzl-Tschegg SE, Tschegg EK. Crack face interaction and mixed mode fracture of wood composites during mode III loading. Eng Fract Mech 1998;61:253–78.
[23] Ehart RJA, Stanzl-Tschegg SE, Tschegg EK. Mode III fracture energy of wood composites in comparison to solid wood. Wood Sci Technol 1999;33:391–405.
[24] Yoshihara H. Examination of the 4-ENF test for measuring the mode III R-curve of wood. Eng Fract Mech 2006;73:42–63.
[25] Li H, Jones RH, Hirth JP. Mixed mode I/III fracture toughness of a V–5Cr–5Ti alloy at 100 °C. Scripta Metall Mater 1995;32(4):611–6.
[26] Kamat SV, Srinivas M, Rao PR. Mixed mode I/III fracture toughness of armco iron. Acta Mater 1998;46(14):4985–92.
[27] Lazarus V, Leblond J-B, Mouschrif S-E. Crack front rotation and segmentation in mixed mode I + III or I + II + III. Part II: comparison with experiments. J Mech Phys Solids 2001;49:1421–43.
[28] Pereira AB, de Morais AB. Mixed mode I + III interlaminar fracture of carbon/epoxy laminates. Compos Part A – Appl Sci 2009;40(4):518–23.
[29] de Morais AB, Pereira AB. Mixed mode II + III interlaminar fracture of carbon/epoxy laminates. Compos Sci Technol 2008;68(9):2022–7.
[30] Szekrényes A. Delamination fracture analysis in the G_{II}–G_{III} plane using prestressed transparent composite beams. Int J Solids Struct 2007;44: 3359–78.
[31] Szekrényes A. Prestressed fracture specimen for delamination testing of composites. Int J Fract 2006;139:213–37.
[32] Szekrényes A. Improved analysis of the modified split-cantilever beam for mode-III fracture. Int J Mech Sci, accepted for publication.
[33] Szekrényes A. Improved analysis of unidirectional composite delamination specimens. Mech Mater 2007;39:953–74.
[34] Rybicki EF, Kanninen MF. A finite element calculation of stress intensity factors by a modified crack closure integral. Eng Fract Mech 1977;9: 931–8.
[35] Szekrényes A, Uj J. Advanced beam model for fiber-bridging in unidirectional composite double-cantilever beam specimens. Eng Fract Mech 2005;72: 2686–702.
[36] Schön J, Nyman T, Blom A, Ansell H. Numerical and experimental investigation of a composite ENF-specimen. Eng Fract Mech 2000;65:405–33.
[37] Hashemi S, Kinloch J, Williams JG. Mechanics and mechanisms of delamination in a poly(ether sulphone)-fibre composite. Compos Sci Technol 1990;37: 429–62.
[38] Hashemi S, Kinloch J, Williams JG. The effects of geometry, rate and temperature on mode I, mode II and mixed-mode I/II interlaminar fracture toughness of carbon-fibre/poly(ether–ether ketone) composites. J Compos Mater 1990;24:918–56.